



Interaction impacts of tides, waves and winds on storm surge in a channel-island system: observational and numerical study in Yangshan Harbor

Zhiguo He¹ · Yanling Tang¹ · Yuezhang Xia¹ · Baode Chen² · Jie Xu² · Zhuzhu Yu¹ · Li Li¹

Received: 28 June 2018 / Accepted: 19 November 2019 / Published online: 3 January 2020
© Springer-Verlag GmbH Germany, part of Springer Nature 2020

Abstract

The Yangshan Deep-Water Harbor (YDH) consists of a northern island chain and a southern island chain, with a deep channel between these two chains. It is frequently impacted by storm tides and waves caused by typhoons. The impacts of the interaction of tide, wave, and wind on storm surges in the channel-island system of the YDH were examined, using field data and a wave-current coupled numerical model, during the super typhoon Chan-hom. Field data showed that the tidal amplitude and currents in the Yangshan area nearly doubled and the current directions were reversed. Surge and significant wave height reached 1.3 m and 8 m, respectively, during the typhoon. Model results agreed well with the observations. Model results revealed that the highest water level occurred at high tide, later than the peak surge, which occurred at low tide. The peak surge occurred at the north coast of the northern island chain, due to the backwater of the chain. The surge in the narrow channel was lower than that in the other areas of the YDH. The current direction in the YDH was slightly southward compared with that during an astronomical tide, due to the winds. A peak surge induced by winds occurred first, followed by wave-induced and the air pressure-induced surges. The wave-induced peak surge occurred at the highest water level. The wind-induced peak surge occurred simultaneously with the peak surge of the storm. Wind has a dominant effect on a storm surge, while wave-current interaction has a minor contribution to the total surge. Wind contributed 87.1% towards the peak surge of the storm, followed by a pressure-induced surge (23.7%) and a wave-induced surge (14.4%), during typhoon Chan-hom.

Keywords Yangshan Harbor · Tide-surge-wave coupling model · Storm tide · Wave · Wind

1 Introduction

The Yangshan Deep-Water Harbor (YDH) is located at the conjunction of the Changjiang River Estuary and Hangzhou Bay. It consists of a northern island chain and a southern island chain, with a deep channel between these two chains (Fig. 1). The northern island and southern island chains constitute a funnel-shaped narrow channel. The water depth in the channel increases from west to east. The width is about 8.1 km, and the depth is about 10 m at the west entrance. The width is 0.9 km at the narrowest part of the east entrance, and the maximum

depth is about 87 m. From 2002 to 2008, a reclamation project was conducted in the Yangshan sea. It closed three tidal channels on the northern island chain and established the offshore YDH (Guo et al. 2018).

The YDH is a hub for the flow and allocation of resources at Shanghai Port. It is vulnerable to storm tide because of its special geographical location. A storm tide refers to the phenomenon whereby sea levels are abnormally increased (or decreased) due to strong atmospheric disturbances such as strong winds and sudden changes in pressure. When a storm tide overlaps with an astronomical high tide, it leads to a sudden rise in the water level, destroying the seawall and causing serious disasters. Therefore, it is of great significance to study the dynamic characteristics of storm tides in the YDH.

A storm tide is accompanied by strong winds, floods, and coastal erosion, which can cause great damage to coastal embankments, ports, and cities (e.g., Fortunato et al. 2017). Storm surges are the main subject of research on storm tides. The magnitude of a surge represents the strength of a storm

Responsible Editor: Lie-Yauw Oey

✉ Yuezhang Xia
yzxia@zju.edu.cn

¹ Ocean College, Zhejiang University, Zhoushan 316012, China

² Shanghai Typhoon Research Institute, China Meteorology Administration, Shanghai 200030, China

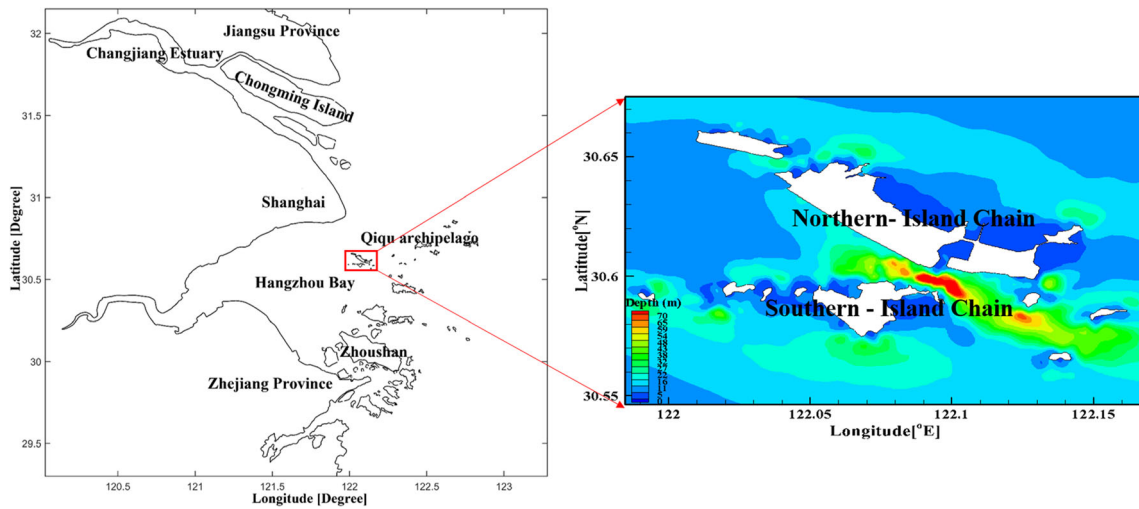


Fig. 1 Map of the Yangshan Deep-Water Harbor

tide. The total surge of a storm tide is related to wave forcing, wind stress, pressure gradient, tide, and water depth (Tolman 2010; Bertin et al. 2015; Zhang and Li, 1996; Xie et al. 2001; Xie et al. 1998; Brown 2010; Sun et al. 2013). Atmospheric pressure makes a large contribution and cannot be ignored, e.g., in the Taiwan Strait (Jiang et al. 1999). The water level in a surge-tide-wave coupling model was found to be more conducive to the forecasting and assessment of storm tides (Zheng 2010). It was found that the linear superposition of an astronomical tide and storm tide overestimated a coupled high tide and underestimated a coupled low tide. The simulation results of storm tides would be improved if wave radiation stress is considered (Liu et al. 2011). Wave, wind stress, and air pressure make various contributions to a storm surge depending on the morphology during a typhoon (Chen et al. 2017). Runoff, precipitation, water density, air pressure, and wave steepness have proved to impact water level during a typhoon (Orton et al. 2012).

In order to study the impacts of the interaction of the main factors (wind, air pressure, and wave) on a storm surge in the YDH, field data of tidal levels, currents, and significant wave heights were measured and analyzed. A tide-surge-wave coupled model was established to examine the contributions of wind, air pressure, and wave on the storm surge.

2 Tide-surge-wave coupling storm tide numerical model

2.1 Model development

2.1.1 FVCOM hydrodynamic model

FVCOM is an unstructured mesh, finite volume, 3D primitive equation ocean model (Chen et al. 2003). It uses an

unstructured triangular mesh in the horizontal direction and a σ coordinate in the vertical direction so that it can be fitted to a complex seabed topography in the vertical direction. The governing equations in the σ coordinate system are as follows:

$$\frac{\partial J u}{\partial x} + \frac{\partial J v}{\partial y} + \frac{\partial A_1 u}{\partial \sigma} + \frac{\partial A_2 v}{\partial \sigma} + \frac{\partial \omega}{\partial \sigma} = 0 \tag{1}$$

$$\begin{aligned} \frac{\partial J u}{\partial t} + \frac{\partial J u^2}{\partial x} + \frac{\partial J u v}{\partial y} + \frac{\partial u \omega}{\partial \sigma} - f v J = & -g J \frac{\partial \zeta}{\partial x} - \frac{J}{\rho_0} \frac{\partial P_a}{\partial x} \\ & - \frac{g J}{\rho_0} \left[\frac{\partial}{\partial x} \left(J \int_{\sigma}^0 \rho d\sigma' \right) + \sigma \rho \frac{\partial J}{\partial x} \right] + \frac{\partial}{\partial \sigma} \left(\frac{K_m}{J} \frac{\partial u}{\partial \sigma} \right) + J F_u \end{aligned} \tag{2}$$

$$\begin{aligned} \frac{\partial J v}{\partial t} + \frac{\partial J u v}{\partial x} + \frac{\partial J v^2}{\partial y} + \frac{\partial v \omega}{\partial \sigma} + f u J = & -g J \frac{\partial \zeta}{\partial y} - \frac{J}{\rho_0} \frac{\partial P_a}{\partial y} \\ & - \frac{g J}{\rho_0} \left[\frac{\partial}{\partial y} \left(J \int_{\sigma}^0 \rho d\sigma' \right) + \sigma \rho \frac{\partial J}{\partial y} \right] + \frac{\partial}{\partial \sigma} \left(\frac{K_m}{J} \frac{\partial v}{\partial \sigma} \right) + J F_v \end{aligned} \tag{3}$$

$$\frac{\partial J \omega}{\partial t} + \frac{\partial J u \omega}{\partial x} + \frac{\partial J v \omega}{\partial y} + \frac{\partial \omega \omega}{\partial \sigma} = \frac{\partial}{\partial \sigma} \left(\frac{K_m}{J} \frac{\partial \omega}{\partial \sigma} \right) + J F_w \tag{4}$$

$$\begin{aligned} \frac{\partial T J}{\partial t} + \frac{\partial T u J}{\partial x} + \frac{\partial T v J}{\partial y} + \frac{\partial T \omega}{\partial \sigma} \\ = \frac{\partial}{\partial \sigma} \left(\frac{K_h}{J} \frac{\partial T}{\partial \sigma} \right) + J \hat{H} + J F_T \end{aligned} \tag{5}$$

$$\frac{\partial S J}{\partial t} + \frac{\partial S u J}{\partial x} + \frac{\partial S v J}{\partial y} + \frac{\partial S \omega}{\partial \sigma} = \frac{\partial}{\partial \sigma} \left(\frac{K_h}{J} \frac{\partial S}{\partial \sigma} \right) + J F_S \tag{6}$$

$$\rho = \rho(T, S) \tag{7}$$

where $J = \partial z / \partial \sigma$, $A_1 = J \partial \sigma / \partial x$, and $A_2 = J \partial \sigma / \partial y$; x , y , and σ are the east, north, and vertical axes; t is time; u , v , and ω are the x , y , and σ components of velocity; T is potential temperature; S is salinity; ρ is density; P_a is air pressure; f is the Coriolis

parameter; K_m and K_h are the vertical eddy viscosity coefficient and the thermal vertical eddy diffusion coefficient; F_u , F_v , F_w , F_T , and F_S represent the momentum, thermal, and salt diffusion terms, respectively; \hat{H} is the solar irradiance.

Wind stress and bottom friction are calculated as surface and bottom boundary condition, respectively. The corresponding boundary conditions are given as follows:

At the sea surface $\sigma = 0$,

$$\left(\frac{\partial u}{\partial \sigma}, \frac{\partial v}{\partial \sigma}\right) = \frac{J}{\rho_0 K_m} (\tau_{sx}, \tau_{sy}), \quad \omega = 0, \tag{8}$$

$$\frac{\partial T}{\partial \sigma} = \frac{J}{\rho c_p K_h} [Q_n(x, y, t) - SW(x, y, 0, t)] \tag{9}$$

At the sea bed $\sigma = -1$,

$$\left(\frac{\partial u}{\partial \sigma}, \frac{\partial v}{\partial \sigma}\right) = \frac{J}{\rho_0 K_m} (\tau_{bx}, \tau_{by}), \quad \omega = 0, \tag{10}$$

$$\begin{aligned} \frac{\partial T}{\partial \sigma} &= -\frac{A_H \tan \alpha}{K_h/J + A_H \tan \alpha} \frac{\partial T}{\partial \sigma} \frac{\partial S}{\partial n}; \quad \frac{\partial S}{\partial \sigma} \\ &= -\frac{A_H \tan \alpha}{K_h/J + A_H \tan \alpha} \frac{\partial S}{\partial \sigma} \frac{\partial S}{\partial n} \end{aligned} \tag{11}$$

where

$$(\tau_{sx}, \tau_{sy}) = \rho C_{ds} \sqrt{u_s^2 + v_s^2} (u_s, v_s) \tag{12}$$

$$(\tau_{bx}, \tau_{by}) = \rho C_{db} \sqrt{u_b^2 + v_b^2} (u_b, v_b) \tag{13}$$

Equations (12) and (13) represent the surface wind stress and bottom stress in the x and y components, respectively; u_s , v_s , u_b , and v_b represent the surface wind velocity and bottom current in the x and y components, respectively; $Q_n(x, y, t)$ is net surface heat flux; $SW(x, y, \zeta, t)$ is the short wave flux in the surface of the sea; A_H is the horizontal thermal diffusion coefficient; α is the bottom slope. The drag coefficient at the surface and the bottom are calculated by

$$C_{ds} = \frac{\kappa^2}{(\ln(10/Z_{0s}))^2}$$

$$C_{db} = \max\left(\frac{\kappa^2}{(\ln(Z_{ab}/Z_{0b}))^2}, 0.0025\right),$$

where Z_{0b} is the bottom roughness parameter and Z_{ab} is the minimum height above the bottom. $\kappa = 0.4$ is the von Karman constant. Z_{0s} is the sea surface roughness used to calculate the wind stress and is calculated by

$$Z_{0s} = 3.7 \times 10^{-5} \frac{U_{10}^2}{g} \left(\frac{U_{10}}{C_p}\right)^{0.9}$$

where U_{10} is the 10-m height wind speed and U_{10}/C_p stands for wave age.

In the calculation of a storm tide, the sea surface wind stress is calculated from the sea surface wind speed (Eq. 12), and then, the wind stress is brought into the numerical model through the upper boundary conditions to calculate the change of wind-driven surface flow (Eq. 8). The turbulent mixing process is considered when calculating the surface flow field, through the vertical eddy viscosity coefficient K_m in Eqs. 2 and 3. The effect of air pressure during a storm tide is considered by the variable P_a in Eqs. 2 and 3. P_a changes with dynamic pressure during a storm tide.

2.1.2 FVCOM-SWAVE wave model

FVCOM-SWAVE (Chen et al. 2006) is an unstructured grid, finite volume, wave model, which has been developed from the third-generation surface wave model SWAN (Simulating Waves Nearshore). The model adopts an implicit method in the calculation procedure, so that its time step is not limited by the CFL condition. The model describes waves based on the Euler approximation wave action density spectrum balance equation. Its governing equation is

$$\frac{\partial}{\partial t} N + \frac{\partial}{\partial x} c_x N + \frac{\partial}{\partial y} c_y N + \frac{\partial}{\partial \sigma} c_\sigma N + \frac{\partial}{\partial \theta} c_\theta N = \frac{S_{tot}}{\sigma} \tag{14}$$

where σ and θ are relative frequency and wave direction in spectral space; x and y are the Cartesian coordinates in geographic space; t is time; N is the wave action density spectrum; c_σ and c_θ are the wave propagation velocities in spectral space; S_{tot} is the source term representing the effects of wind-wave generation, wave breaking, bottom dissipation, and nonlinear wave-wave interactions.

2.1.3 Model coupling

Waves affect the circulation of water through radiation stresses and sea surface wind stress, and a change of sea surface water level will affect the calculation of waves. FVCOM-SWAVE uses the same unstructured mesh as the FVCOM hydrodynamic model. The wave model calculates significant wave height (H_s), wave direction (Dir), wave length (L), peak period (T_p), bottom orbit velocity (U_b), and bottom wave period (T_b). Subsequently, the values of radiation stress and the sea surface stress are transmitted to the hydrodynamic model. The hydrodynamic model calculates the water level, velocity, and other variables and feeds them back to the wave model for the calculation of the wave parameter for the next step. After the hydrodynamic model and the wave model complete a calculation, the wave parameters and flow field data are

transferred to the bottom boundary layer model (BBL), and subsequently the bottom stress (τ_b) is calculated. Please refer to the FVCOM user manual for the detailed information of the BBL model (Chen et al. 2013). The calculated stress is then transmitted to the hydrodynamic model to update the momentum equations. Figure 2 shows the transfer of the coupling model variables.

The equations in the tide-wave coupled model were shown in the σ coordinate as follows (Wu 2009). The continuity equation is

$$\frac{\partial DU_\alpha}{\partial x_\alpha} + \frac{\partial \Omega}{\partial \varsigma} + \frac{\partial \eta}{\partial t} = 0,$$

and the momentum equation is

$$\begin{aligned} & \frac{\partial}{\partial t}(DU_\alpha) + \frac{\partial}{\partial x_\beta}(DU_\alpha U_\beta) + \frac{\partial}{\partial \sigma}(\Omega U_\alpha) - \varepsilon_{\alpha\beta\gamma} f_\gamma DU_\beta \\ & + D \frac{\partial}{\partial x_\alpha}(g\eta + p_{\alpha tm}) + D \int_\sigma^0 \left(D \frac{\partial b}{\partial x_\alpha} - \varsigma \frac{\partial D}{\partial x_\alpha} \frac{\partial b}{\partial \sigma} \right) d\sigma \\ & = - \frac{\partial DS_{\alpha\beta}}{\partial x_\beta} + \varsigma \frac{\partial D}{\partial x_\beta} \frac{\partial S_{\alpha\beta}}{\partial \sigma} + \frac{\partial \tau_\alpha}{\partial \sigma}, \end{aligned}$$

where the first term is the local term, the second and the third terms on the left are the advection process, the fifth and sixth terms on the left are the barotropic and baroclinic pressure gradient terms, $p_{\alpha tm}$ represents the pressure, $S_{\alpha\beta}$ is the wave radiation stress, and τ_α is the surface wind stress. More details on model coupling are referred to in the FVCOM User Manual (Chen et al. 2012) and Wu (2010).

The coupled model was applied to study the impacts of super typhoon Chan-hom on tidal level, currents, and significant wave height in the YDH.

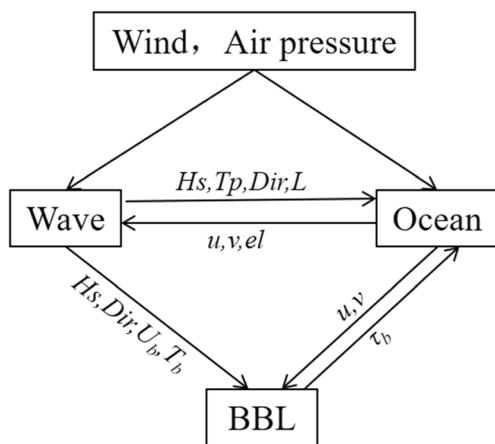


Fig. 2 Variable transfer scheme in the coupled model. Wind and air pressure represent the input of wind data and air pressure data. Wave represents the wave model. Ocean represents the hydrodynamic model. BBL represents the bottom boundary layer model. u , v , and el are velocity and water levels

2.2 Model configurations

2.2.1 Characteristics of super typhoon Chan-hom

Super typhoon Chan-hom was named 09W by the Joint Typhoon Warning Center after a low-pressure zone in the western Pacific Ocean became a tropical depression at 0 p.m. on June 30, 2015 (UTC time, 8 p.m. on June 30 local time, as below). It advanced northwestwards after formation and strengthened into a typhoon on July 7. At 3 p.m. on July 9, Chan-hom strengthened into a super typhoon and continued to move west-northwestwards. Its peak intensity occurred at 4 a.m. on July 10. The maximum wind speed near the typhoon eye reached 58 m/s, and the central pressure was 925 hPa, showing how exceptional this event was. After weakening into a strong typhoon at 2 a.m. on July 11, it made landfall at Zhujiajian (Fig. 1) at 8:40 a.m. The maximum wind speed reduced to 45 m/s, and the minimum pressure at the typhoon eye was 955 hPa. Then, its direction turned to north-northeast, and its intensity began to weaken. It passed through the East China Sea and the Yellow Sea, and eventually made landfall on the southwestern part of North Korea on July 13, where it weakened. The path of typhoon Chan-hom and the corresponding pressure at its eye (hPa) are shown in Fig. 3. The

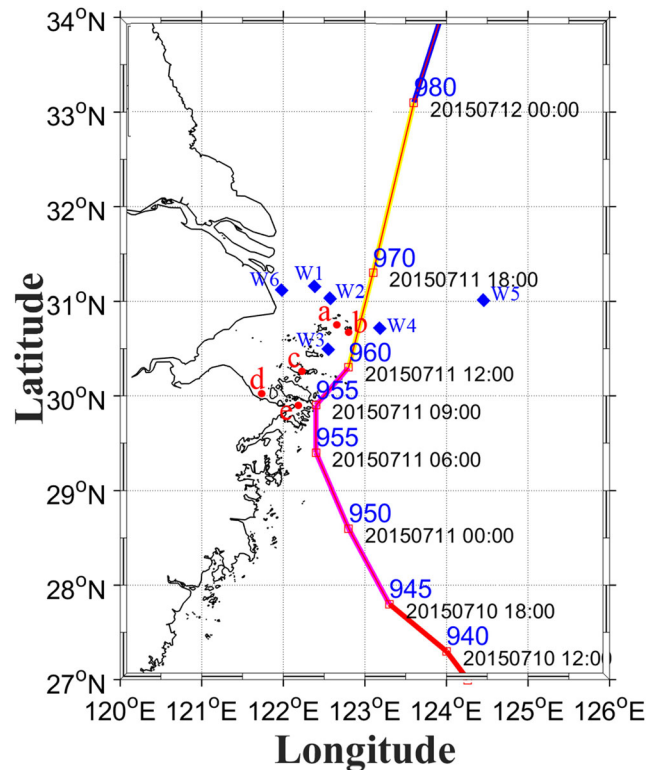


Fig. 3 Path of typhoon Chan-hom and the location of model verification station. a–e stations are for water level. W4 station is for current. W1 to W5 stations are for significant wave height. The blue numbers indicate pressure at the typhoon eye. The black numbers are date and time

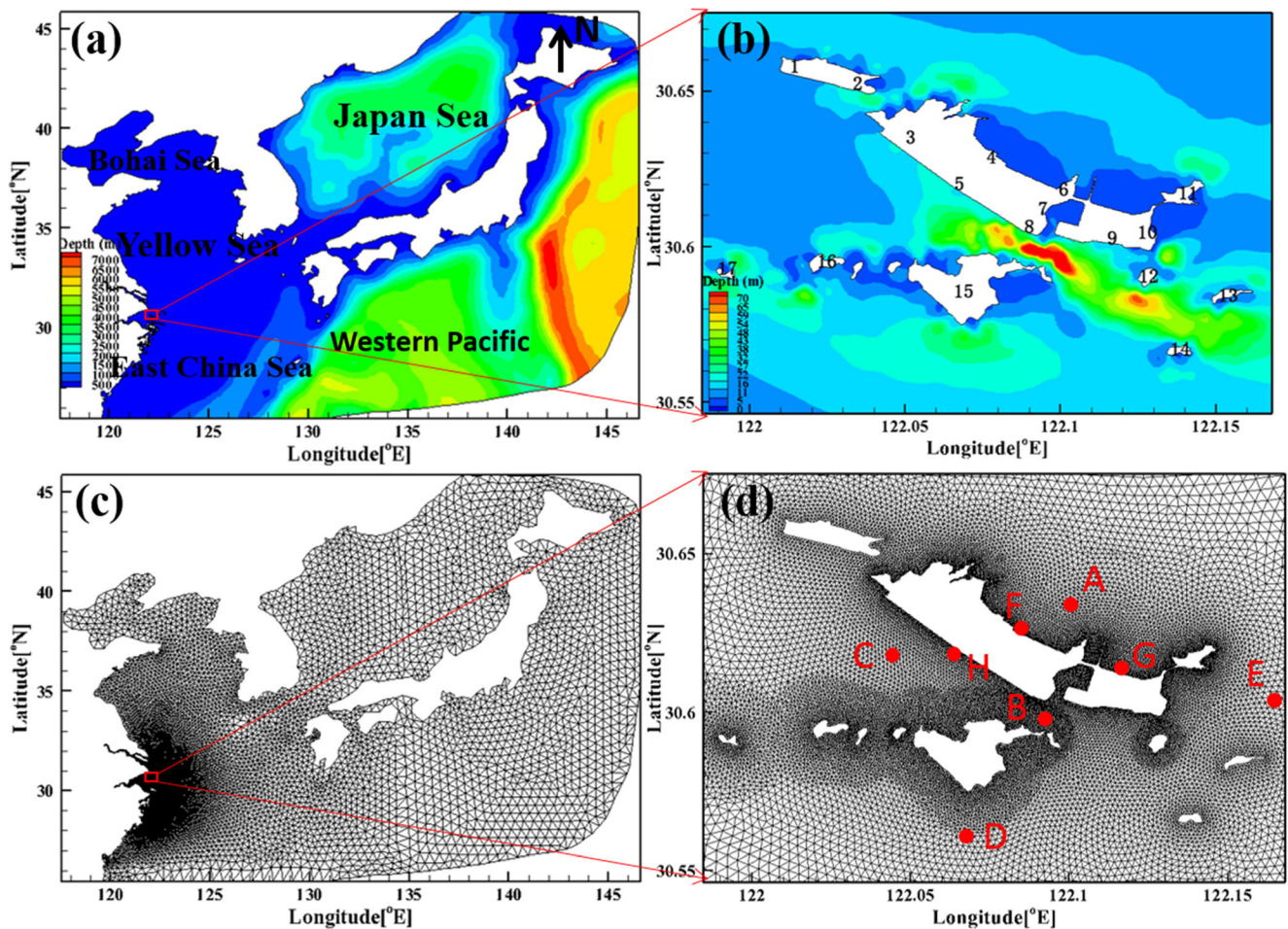


Fig. 4 **a** Bathymetry of the model domain. **b** Bathymetry of the Yangshan Deep-Water Harbor (YDH): (1) Dawugui, (2) Kezhushan, (3) Xiaoyangshan, (4) Jiangjunmao, (5) Huogaitang, (6) Dazhitou, (7) Dayanjiao, (8) Xiaoyanjiao, (9) Zhongmentang, (10) Shenjiawan, (11) Baodaozui, (12) Shaoji, (13) Huxiaoshe, (14) Maanshan, (15)

Dayangshan, (16) Dashantang, and (17) Shuanglianshan. **c** Grids of the model domain. **d** Grids of the YDH. Locations of A–H in **d** are selected to show the characteristics of water levels, currents, and significant wave heights in the YDH

data were taken from the China Typhoon Network (www.typhoon.gov.cn) (Ying et al. 2014).

2.2.2 Model domain and configuration

The model domain covers 117°–146° E, 25°–46° N, including the western Pacific, Japan Sea, Bohai Sea, Yellow Sea, and East China Sea (Fig. 4a). This domain fully contains the main progress of typhoon Chan-hom. The bathymetry data were obtained from ETOP1 terrain data provided by NOAA with a resolution of 1 min (<https://ngdc.noaa.gov/mgg/globalglobal.html>). Regional shoreline data were obtained from NGDC (<https://www.ngdc.noaa.gov/mgg/shorelines/gshhs.html>). The bathymetry data of the harbor were obtained from the latest charts in 2015 provided by the Maritime Affairs Bureau. The water depth between Dayangshan and Xiaoyangshan varies considerably along the straight line (Fig. 4b). The water depth is 87 m at the narrow channel (Xiaoyanjiao–Dayangshan section) and

rapidly reduces to about 10 m at the Kezhushan–Dashantang section. The variability of the depth in the west of the Kezhushan–Dashantang section is relatively small. The computational domain includes 93,363 nodes and 175,917 triangular elements. Ten uniform sigma layers are applied to the vertical direction. In order to improve computational efficiency, the sizes of the grids are ranged from about 50 km at the open boundary (Fig. 4c) to 50 m in the harbor. The water depth in the YDH has large variations, and the coastline is complicated near the islands; hence, high-resolution grids are applied to ensure calculation accuracy (Fig. 4d).

The model was forced by the hourly tide-level data of eight tidal components ($K_1, O_1, P_1, Q_1, M_2, S_2, N_2, K_2$) specified at the open boundaries. The harmonic constant of each tidal component was obtained from the global tidal model TPXO (Pawlowicz et al. 2002; Egbert et al. 1994; Egbert and Erofeeva 2002). Runoff from the Changjiang River and the Qiantang River was taken into account in the model. The discharge of the Changjiang River was obtained from the

Table 1 Model configuration

Model parameters	Parameter configuration
Model domain	E 117°~E 146°, N 25°~N 46°
Resolution	Maximum grid size 50 km, minimum grid size 50 m
Number of nodes, elements, and vertical sigma levels	93,363 nodes, 175,917 elements, 10 sigma layers
Model time	June 28, 2015–July 15, 2015
Time step of hydrodynamic model	External time step 0.2 s, internal time step 2 s
Time step of wave model	2 s
Spectral resolution	20 × 36 (frequency × direction)
Boundary condition	Runoff: Datong, Fuchunjiang Tidal forcing: $M_2, S_2, K_1, O_1, N_2, P_1, Q_1, K_2$
Initial condition	Cold start (water level, current, and wave were 0, temperature 20°, salinity 30‰)
Wind data	ECMWF wind data, with temporal and spatial resolution of 6 h and 0.125°, respectively
Air pressure	NCEP-FNL pressure data, with temporal and spatial resolution of 6 h and 1°, respectively

Datong hydrometric station and obtained from the water-level management system (<http://yu-zhu.vicp.net/>); the flux of the Qiantang River was from the Fuchunjiang hydrology station. Wind data is the reanalysis data provided by the European Centre for Medium-Range Weather Forecasts (ECMWF) (<http://apps.ecmwf.int/datasets/data/interim-full-daily/levtype=sfc/>). The temporal resolution of wind data is 6 h, and the spatial resolution is 0.125°. The air pressure data were also obtained from ECMWF, with spatial resolution of 1° and temporal resolution of 6 h.

The model time was from June 28 to July 15, 2015. The initial current and water levels for the model were set to 0. The initial temperature was set to 20°, and the initial salinity was set as 30‰. The external time step was set to 0.2 s, and the internal time step was set to 2 s. The initial error was basically eliminated after 3 days of model running. The modeled data from June 30 to July 14 were used for result analysis. The initial condition for wave was set to 0. The temperature and salinity were initialized as 20° and 30‰, respectively. The configuration of the model is shown in Table 1.

2.2.3 Numerical tests

Five numerical experiments were designed to quantify the contributions of air pressure, wind, and wave to a storm surge (Table 2) based on the tide-surge-wave coupled numerical model. Case 0 is the reference case described above. Case 1 excluded wave radiation stress to test the contribution of wave on the total surge. Case 2 ignored wind speed to test the impacts of wind on the total surge. Air pressure was removed in case 3 to examine the impacts of air pressure on total surge. Case tide considered only the astronomical tide to calculate the total surge during typhoon Chan-hom.

3 Model validation

3.1 Verification of water level and current

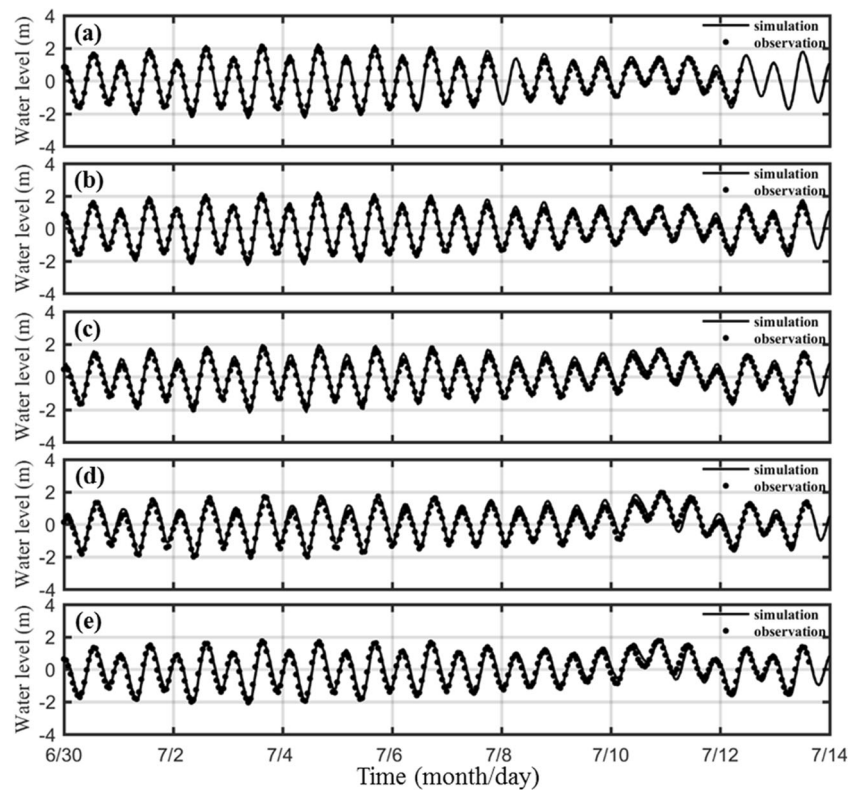
The water level (Fig. 5) and vertical-average current (Fig. 6) data from June 30 to July 14, 2015 were used to validate the

Table 2 Descriptions of numerical tests

Cases	Factors					Descriptions
	Tide	River	Wind	Air pressure	Wave	
Case 0	√	√	√	√	√	Reference
Case 1	√	√	√	√		Wave-induced surge
Case 2	√	√		√	√	Wind-induced surge
Case 3	√	√	√		√	Air pressure-induced surge
Case tide	√					Total surge
Case R1	√	√	√	√	√	Reconstructed wind

√ indicates that the parameter is included in the numerical test

Fig. 5 Comparison of simulated and observed water levels. a–e Stations a to e (Fig. 3)



model. The locations of field stations are shown in Fig. 3. The measured data used in this paper were provided by the Shanghai Meteorological Service, the Center for Numerical Prediction and Innovation, and the Zhejiang Marine Monitoring and Forecasting Center. The accuracy of model predictions was evaluated using *Skill* values (Willmott 1981; Warner et al. 2005). The *Skill* value is calculated by

$$Skill = 1 - \frac{\sum_{i=1}^N |X_{mod} - X_{obs}|^2}{\sum_{i=1}^N (|X_{mod} - \bar{X}_{obs}| + |X_{obs} - \bar{X}_{obs}|)^2}. \quad (15)$$

X_{mod} and X_{obs} are the simulated values and the measured values, respectively. The \bar{X}_{obs} is the time-averaged values of the measured data. The value of *Skill* is between 0 and 1,

which indicates that the measured values are completely consistent (*Skill* = 1) or inconsistent (*Skill* = 0) with the simulated values.

The *Skill* values of the water level and current at each station are shown in Table 3. The *Skill* values of most of the stations were larger than 0.9, indicating that the modeled water level and current results agreed well with the measured data. The model well reproduced the storm tide during typhoon Chan-hom.

3.2 Verification of significant wave height

The model used the simulated and observed significant wave height data from June 30 to July 14, 2015 to verify the performance of the model in simulating waves (Fig. 7). The model well reproduced the magnitudes and trends of the significant

Fig. 6 Comparison of simulated and observed vertical averaged tidal currents at station W4 (Fig. 3)

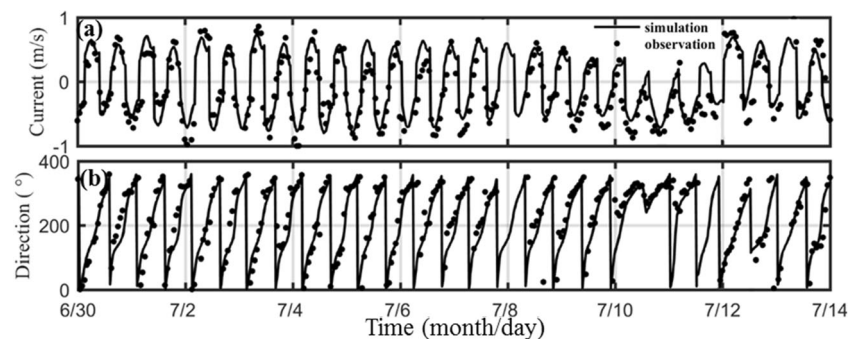


Table 3 The *Skill* values of water level and tidal current at all field stations

	Water level					Tidal current (station W4)	
	Station a	Station b	Station c	Station d	Station e	Speed	Direction
<i>Skill</i>	0.99	0.99	0.99	0.98	0.98	0.90	0.85

wave heights at all five field stations. The *Skill* values at all field stations were larger than 0.9 (Table 4), showing that the simulated significant wave height results were in good agreement with the measured values.

4 Results

4.1 Storm surge measurements

Water levels at stations a to e, current speeds and directions at station W4, and significant wave height at stations W1 to W5 (Fig. 3) were measured during typhoon Chan-hom (Fig. 4). The response of tides and waves in the YDH to the passing of typhoon Chan-hom was a short episodic event. The effect of the storm perturbed the tidal level, current structure, and waves for about 72 h before the seasonal climatology returned.

Measured water level data at the five stations showed that the maximum high water level and the minimum low water level reached 2 m and -2 m, respectively, during the neap

tides between July 11 and 13 during typhoon Chan-hom (Fig. 5). These tidal levels were as high/low as those during spring tides at the five stations.

The current speeds were almost double those during astronomical neap tides between July 11 and 13 (Fig. 6a). The maximum vertical averaged current speed was almost 1 m/s. The current directions were even reversed during the typhoon (Fig. 6b).

Typhoon Chan-hom also generated large waves as it propagated up the coast. The significant wave heights (H_s) were higher than 4 m at all field stations on July 11 (Fig. 7). Lower peaks of H_s of more than 2 m were captured at all field stations on July 7. A peak H_s of about 8 m occurred at stations W4 and W5 (Fig. 7d, e). The largest waves coincided with the northward current event immediately following the passage of the typhoon eye.

4.2 Storm surge in Yangshan Harbor

The total storm surge during typhoon Chan-hom was calculated by comparing the differences of tidal levels between the

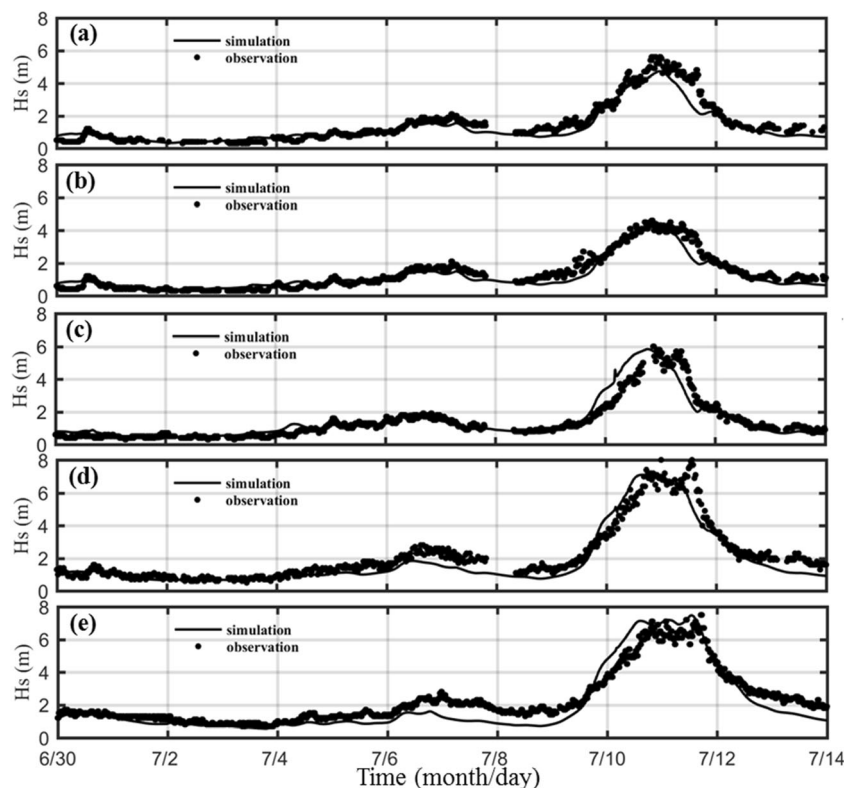
Fig. 7 Comparison of modeled and observed significant wave heights. a–e Stations W1 to W5

Table 4 The *Skill* values of significant wave height at verification sites

Site	Station W1	Station W2	Station W3	Station W4	Station W5
<i>Skill</i>	0.97	0.97	0.96	0.97	0.96

reference case (case 0) and case tide (Table 4). Eight sites (A to H, Fig. 4d) around the YDH were selected to analyze the storm surge at different locations.

The water levels of the reference case (case 0, black solid line) and case tide (blue dotted line) at the A–H sites and their differences (total storm surge, red dotted line) are shown in

Fig. 8. Typhoon Chan-hom made landfall in the Yangshan sea area (at Zhujiajian, Fig. 1) during the neap tide, when the predicted tide level for the low high tide/high high tide was 1.16 m/1.31 m, respectively. The highest water level appeared at 10 p.m. on July 10 (11 h before landfall) at the A–H sites, at the time of the astronomical high tide. The highest water levels were 1.91 m, 1.85 m, 1.91 m, 1.89 m, 1.81 m, 2 m, 1.99 m, and 1.90 m, respectively, at the A to H sites. Due to the small area of the YDH and the location of the sites, the highest water levels of the eight sites were almost the same. Due to their locations, the maximum and minimum values of highest water level occurred at point F and point E, respectively. Point F is at the front of the northern island chain and affected by the

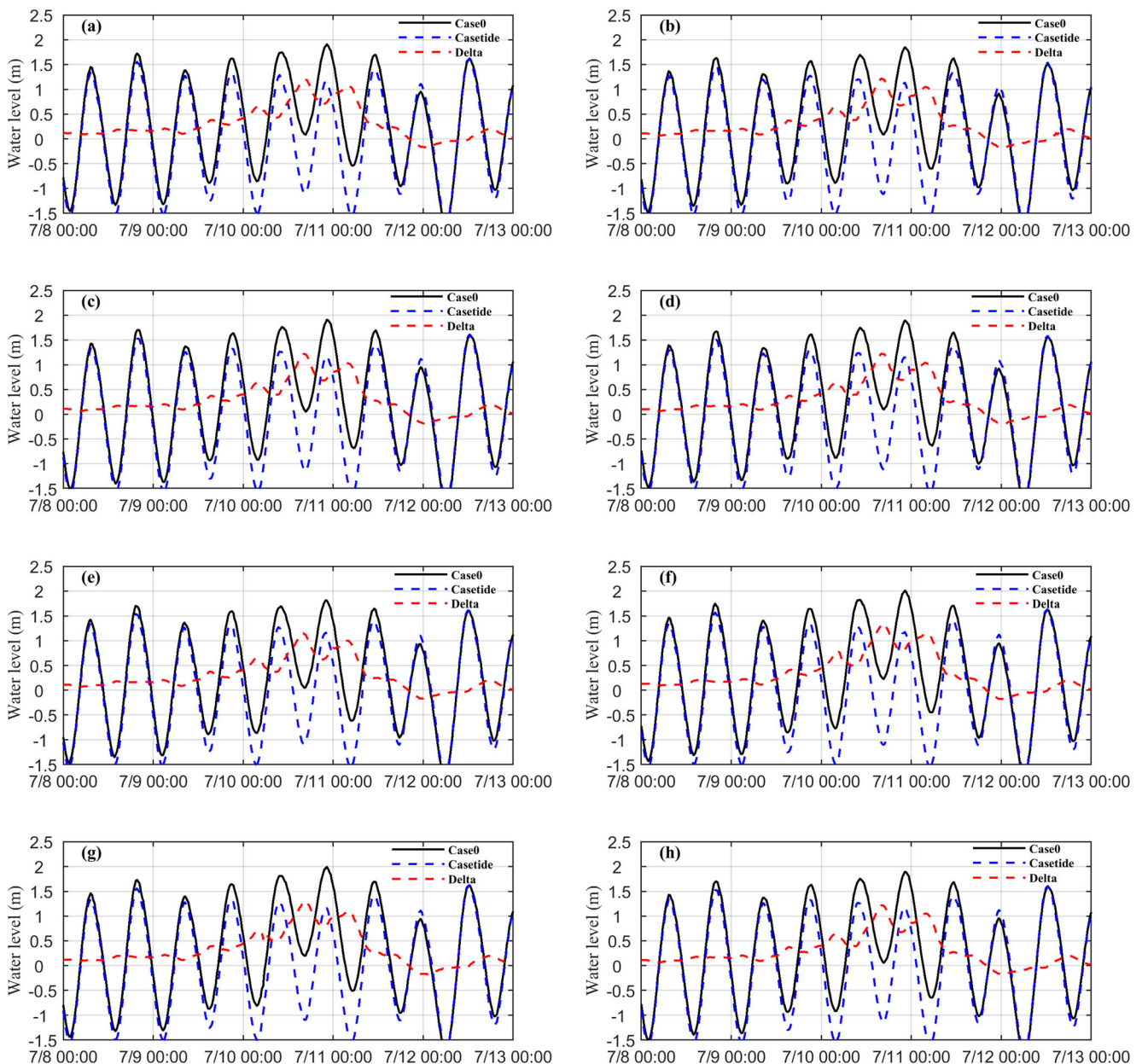


Fig. 8 Water levels of case 0 (black line), case tide (blue line), and total surge (red line). **a–h** Sites A to H

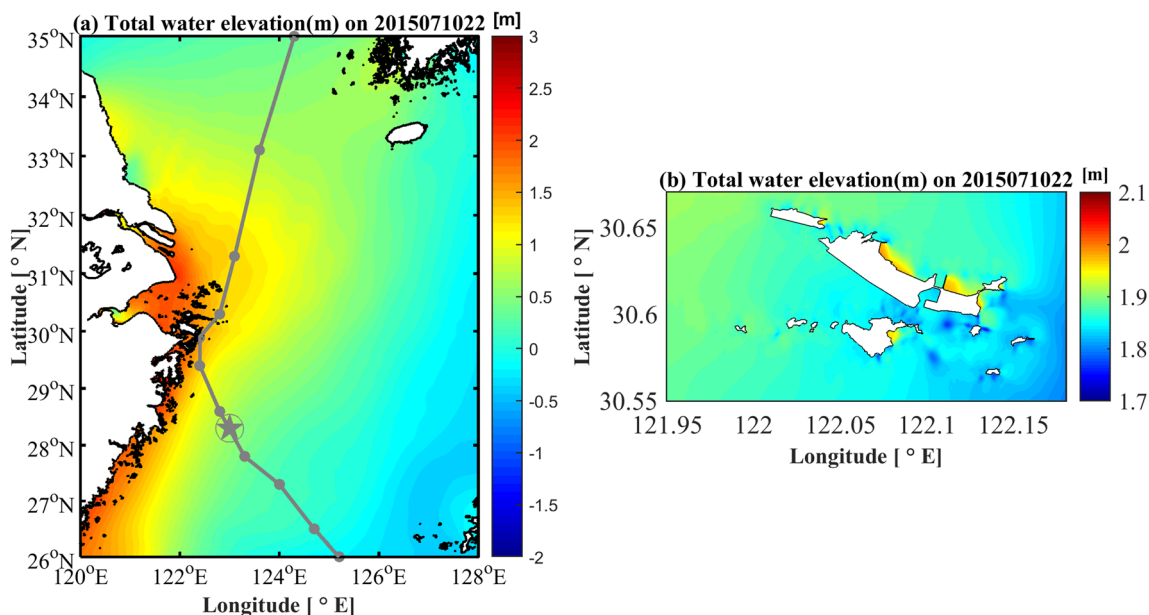


Fig. 9 Spatial distribution of the total water level when the peak total water level in the YDH occurred: **a** entire model domain and **b** YDH

backwater of the islands, while point E is close to the open sea and is less affected by the islands.

The peak surge of storm tide in the Yangshan sea area occurred at 4 p.m. on July 10 (17 h before landfall). This is because the location of the Yangshan sea area was at the maximum wind speed radius of typhoon Chan-hom, and it was at a high low tide at that time. The total storm surges at the A to H site were 1.20 m, 1.22 m, 1.22 m, 1.23 m, 1.15 m, 1.34 m, 1.30 m, and 1.22 m, respectively. The largest storm surge occurred at site F due to the backwater by the northern island chain. The highest water level occurred later than the peak

surge. The highest water level occurred at the time of the astronomical high tide, but the peak surge appeared at the time of the low tide.

The highest total water level (case 0) in the YDH appeared at 10 p.m. on July 10 (11 h before landfall). The spatial distributions of the total water level in the entire model domain and the YDH at this time are shown in Fig. 9. After the tidal waves from the Pacific Ocean propagated into the East China Sea, most of them continued to spread to the Yellow Sea. Only a small part of the tides entered Hangzhou Bay and the Changjiang River Estuary. The water level on the west side

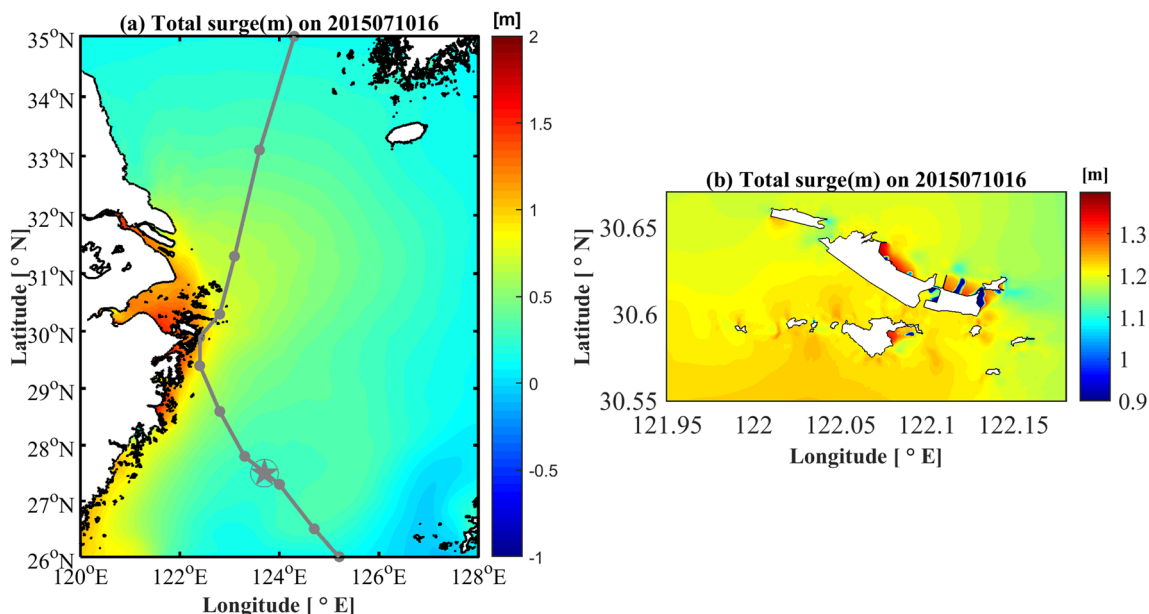


Fig. 10 Spatial distribution of the total surge when the peak surge in the YDH occurred: **a** entire model domain and **b** YDH

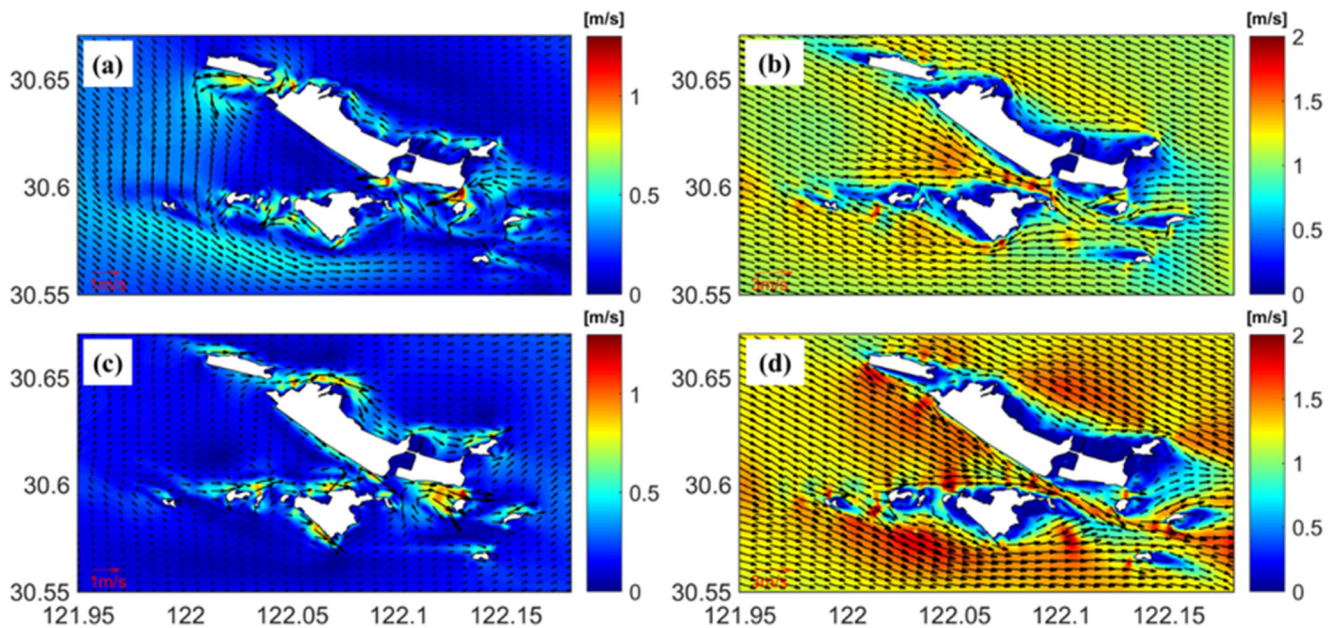


Fig. 11 Surface current field of astronomical tide during the neap tide in the YDH. **a** Low slack water (6 p.m. on July 10), **b** flood tide (9 p.m. on July 10), **c** high slack water (0 p.m. on July 11), and **d** ebb tide (3 a.m. on

July 11). Color represents the magnitude of current, and the arrow represents the direction of current

of the YDH was higher than that on the east side. Due to the backwater by the chain, the water level near the shore was higher than that in the open sea, and the total water level in Hangzhou Bay was slightly higher than that in the other areas. The highest water level in the YDH was about 2.27 m, which was about twice that of the forecasted tide level at that time.

The peak surge in the YDH appeared at 4 p.m. on July 10 (17 h before landfall, Fig. 10). The spatial distributions of the storm surge in the entire model domain and the YDH at this time are shown in Fig. 10. The surge on the western side of the YDH was slightly higher than that on the eastern side (about 0.2 m). The maximum surge was

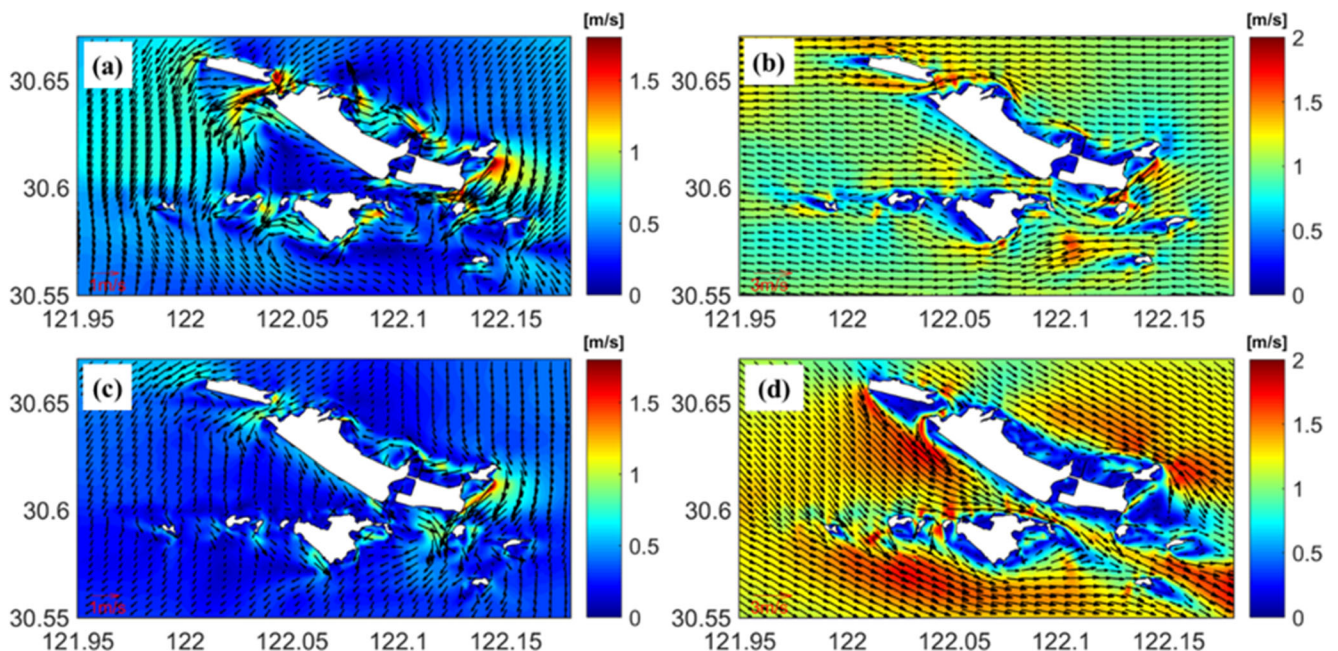


Fig. 12 Surface current field of storm tide during neap tide in the Yangshan sea area. **a** Low slack water (6 p.m. on July 10), **b** flood tide (9 p.m. on July 10), **c** high slack water (0 p.m. on July 11), and **d** ebb tide

(3 a.m. on July 11). Color represents the magnitude of current, and the arrow represents the direction of current

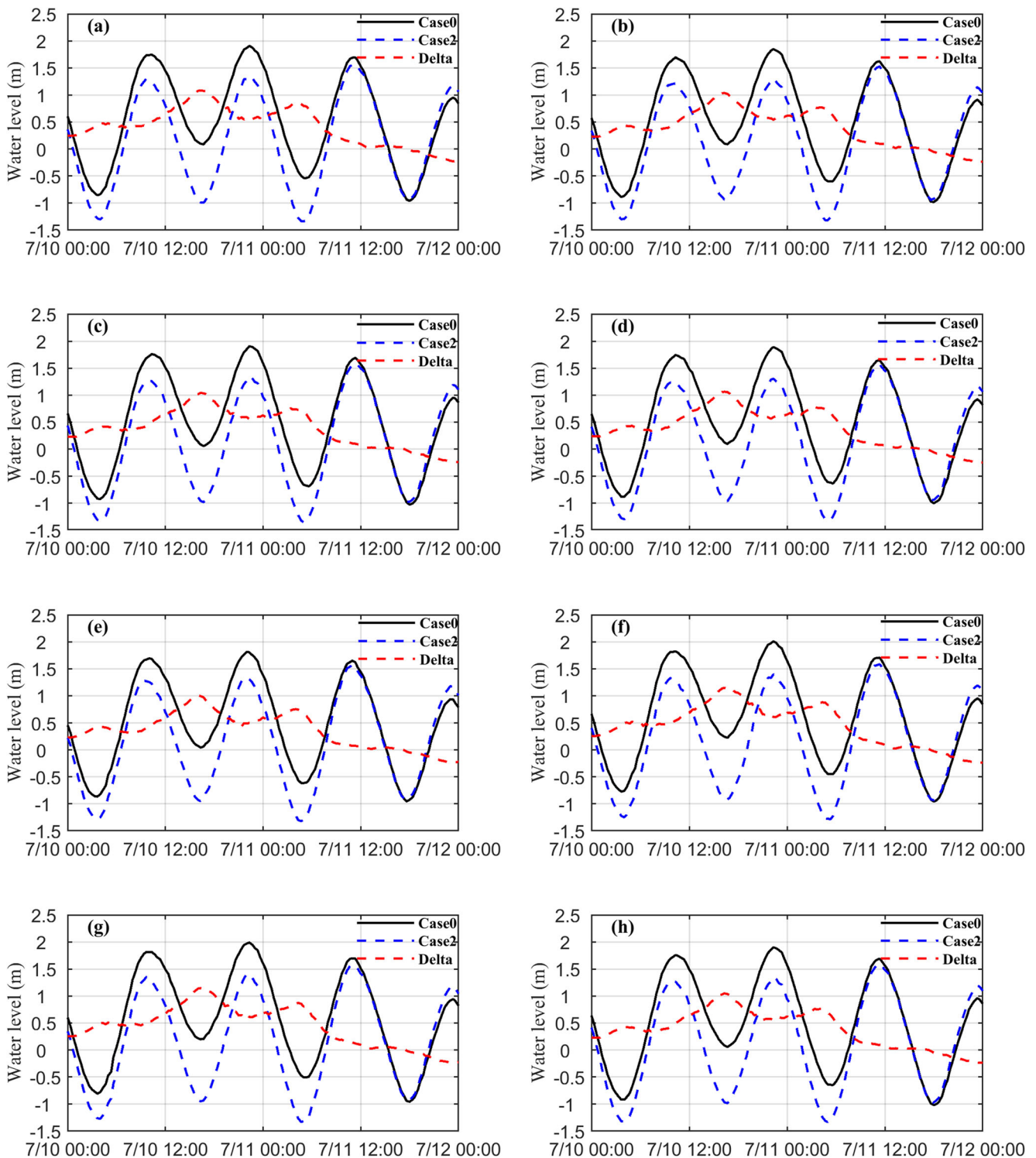


Fig. 13 Water levels of case 1 (black line), case 2 (blue line), and wind-induced surge (red line). **a–h** Stations A to H

1.52 m, which occurred on the northern shore of the north island chain. There is a blue band-shaped area in the middle of the concave shore on the east side of the north island chain, where the surge was smaller than the surrounding area due to shallow water depth.

The highest water levels and the maximum surge of the storm tides in the Yangshan sea area all occurred on the northern shoreline of the north island chain during typhoon Chan-hom. Thus, it is important to protect this area from future storm tides.

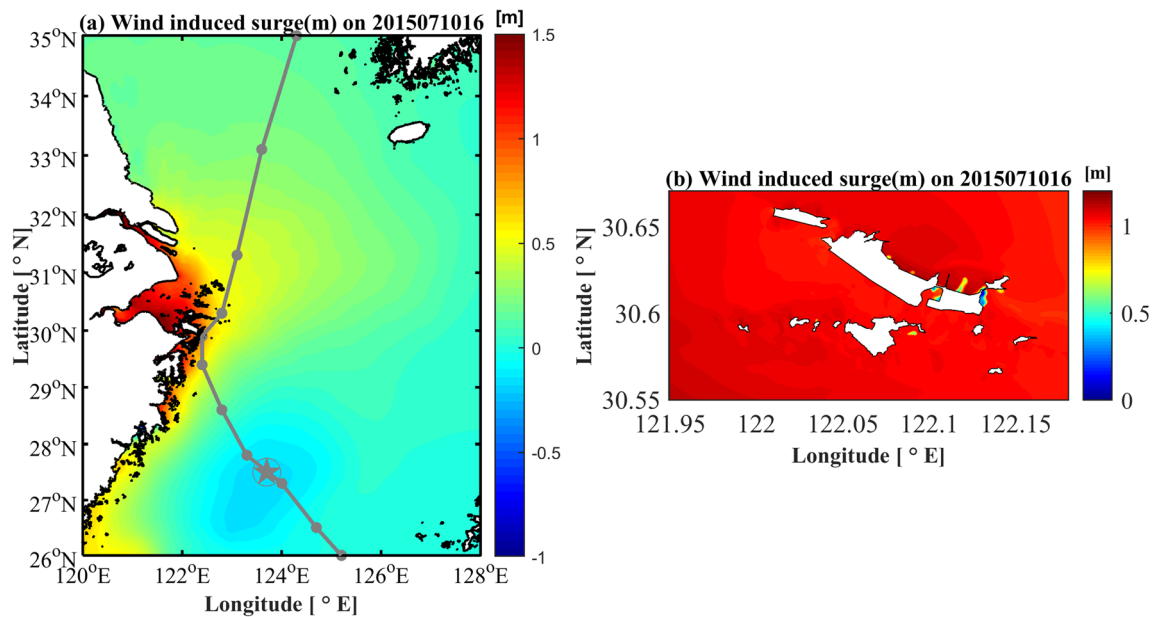


Fig. 14 Spatial distribution of maximum wind-induced surge on 4 p.m. July 10: **a** entire model domain and **b** YDH

4.3 Impacts of storm tide on currents in YDH

The surface currents during neap tides in case tide (forcing by astronomical tides) are shown in Fig. 11.

At the flood tide (Fig. 11b), some of the tidal waves from the open sea pass through the channel between Huxiaoshe Island and Maanshan Island (see Fig. 4b for locations). The remainder propagates through the channel between Shenjiawan Island and Shaoji Island to enter the Yangshan sea area. The current speed in the tidal channels in the YDH is increased due to the effect of tidal choking.

At the ebb tide (Fig. 11d), the current direction is basically in the opposite direction to the flood current. Part of the water ebbs through the tidal channel between Kezhushan Island and Xiaoyangshan Island, while most of the water ebbs through the deep channel between the two island chains. After that, the ebb tide branches into two channels and finally joins the water in the East China Sea. One channel goes between Huxiaoshe Island and Maanshan Island, and the other channel goes between Shenjiawan Island and Shaoji Island.

The surface currents at the same tidal cycle during neap tides when typhoon Chan-hom made landfall (reference case 0) are shown in Fig. 12.

The surface currents during the typhoon were deflected in comparison with those during astronomical tides, due to strong northeast winds. At the ebb slack time, the current between the Kezhushan and Xiaoyangshan channels was strengthened (Fig. 12a). During the flood time, the flood current was deflected to the west. The flood tide increased in the channels (Fig. 12b) between Kezhushan Island and Xiaoyangshan Island, and Shenjiawan Island and Shaoji Island (see Fig. 4b for location), compared with the

astronomical tide current (Fig. 11b). In general, the flood current in the Yangshan sea area had been weakened. At the flood slack time (Fig. 12c), the Yangshan sea area was dominated by the northeast to southwest current fields. Under the influence of a slight ebb current on the east side of the sea area (Fig. 12c), a southward current appeared. At the ebb tide (Fig. 12d), the current directions were slightly deflected to the south due to the northeast wind, compared with that during the astronomical tide (Fig. 11d). The tidal choking effect was weakened at the narrow channel during flood and ebb time due to the storm tide.

5 Discussions

5.1 Contribution of winds to the storm surge in the YDH

The wind-induced surge was evaluated by comparing the water levels between case 2 and case 1. Figure 13 shows the water levels of case 1 (black solid line) and case 2 (blue dotted line) and their differences (wind-induced surge, red dotted line) at A to H sites (Fig. 4d).

The wind-induced surge in the YDH reached its peak at 4 p.m. on July 10 (17 h before landfall), when the YDH was situated at the maximum wind speed radius of the typhoon eye. The magnitudes of the surges at the A to H sites were generally the same. The wind-induced surges at the A to H sites were 1.04 m, 1 m, 1 m, 1 m, 0.96 m, 1.11 m, 1.10 m, and 1.01 m and were 87.1%, 82.1%, 81.8%, 83.7%, 82.8%, 83.2%, 84.4%, and 82.6% of the total storm surge, respectively. The surge at site F was the

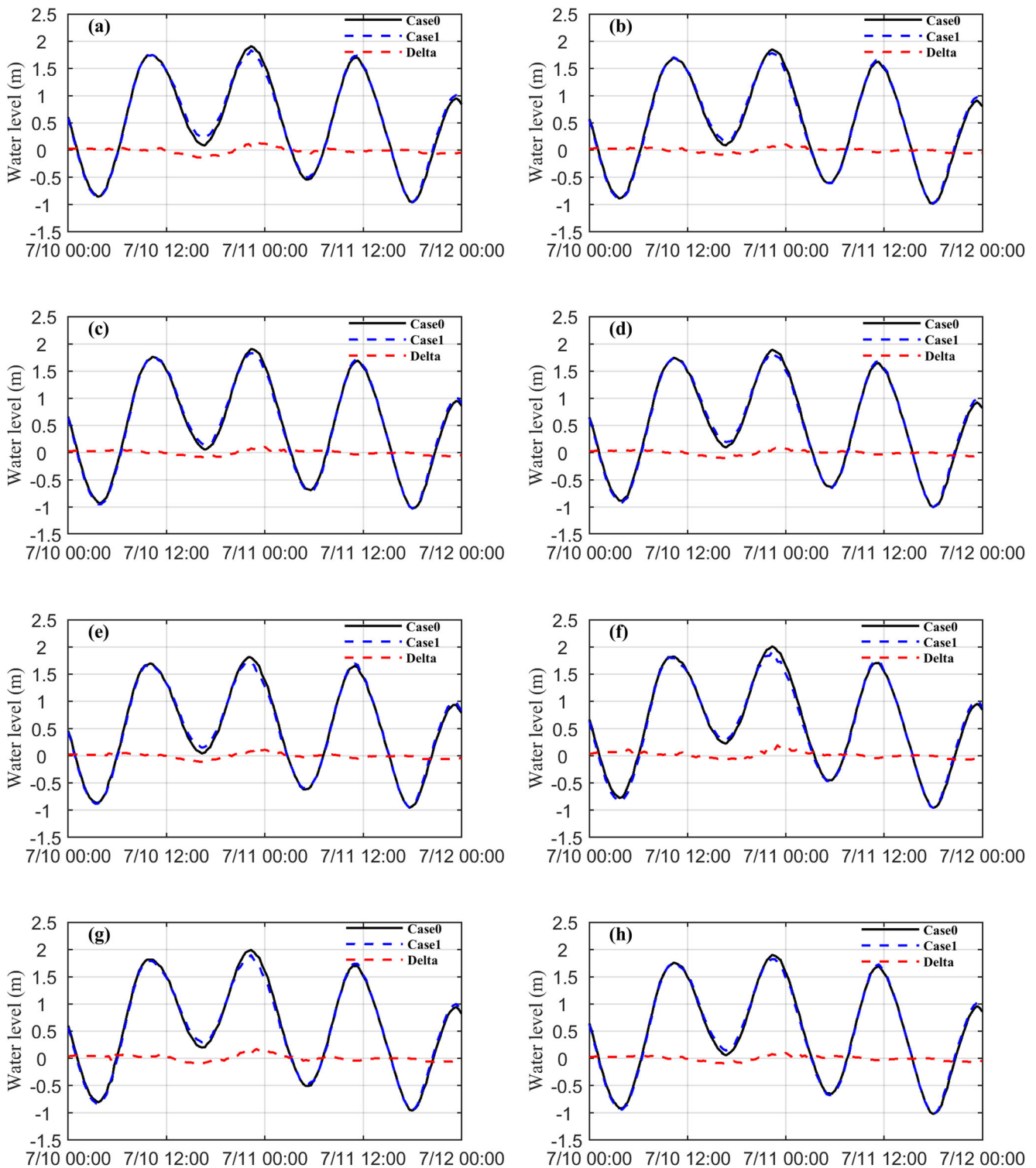


Fig. 15 Water levels of case 0 (black line), case 1 (blue line), and wave-induced surge (red line). **a–h** Stations A to H

largest, and that at site E was the smallest. The cyclone eye was located on the south side of the YDH, and the wind direction was northeast. Site F was on the northern bank (concave coast), where the water was blocked by the north island chain, and so, the surge was amplified.

The influence of the wind on the storm tide of Yangshan Harbor is crucial. The moment of peak wind-induced surge coincided with the peak total surge, which indicated that the storm surge was mainly caused by the wind during typhoon Chan-hom.

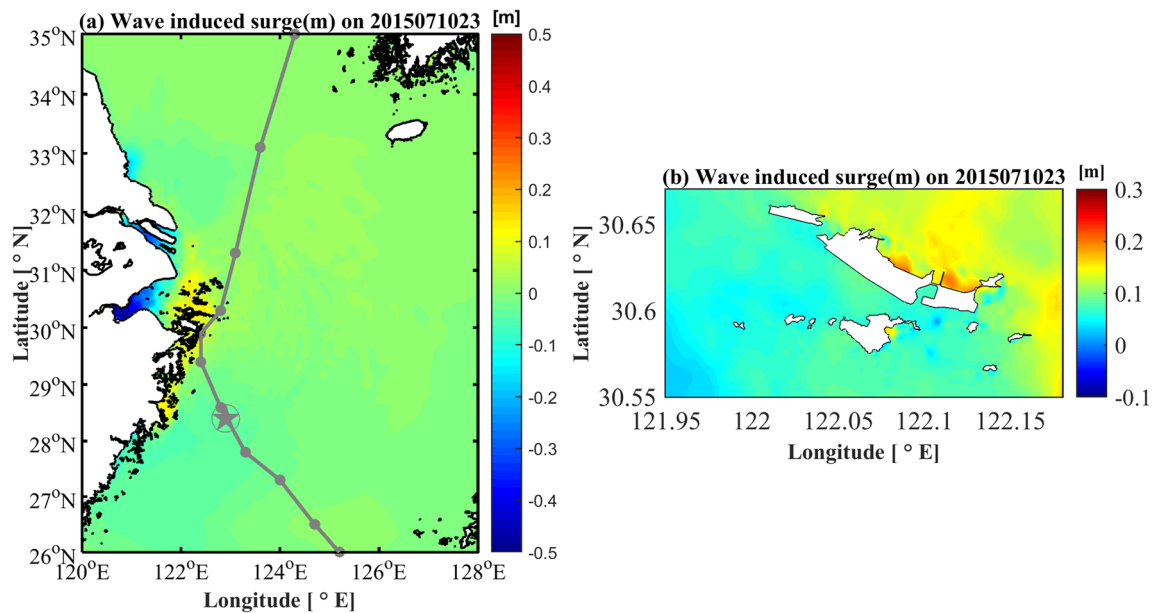


Fig. 16 Spatial distribution of maximum wave-induced surge on 11 p.m. July 10: **a** entire model domain and **b** YDH

The peak wind-induced surge in the YDH occurred at 4 p.m. on July 10 (17 h before landfall). The spatial distributions of the wind-induced surge in the entire model domain and the YDH at this time are shown in Fig. 14. There was a rise in water level in Hangzhou Bay, but a decrease in water level near the eye of typhoon Chan-hom. The peak wind-induced surge was about 1.25 m. The surge at the northern bank of the north island chain was greater than that at the southern bank of the south island chain, due to the northeasterly winds. The surge in the trumpet-shaped channel between the north and south island chains was smaller than that in other areas due to the block of the channel-island system.

5.2 Contribution of waves to the storm surge in YDH

The wave-induced surge was evaluated by comparing the water levels of case 0 (reference model) and case 1 (without wave). Figure 15 shows the water level in case 0 (black solid line) and case 1 (blue dotted line) and the differences (wave-induced surge, red dotted line) at the A to H sites (Fig. 4d).

The wave-induced surge in the YDH peaked at 11 p.m. on July 10 (10 h before landfall). The wave-induced surge at the A–H sites was 0.15 m (12.3%), 0.11 m (8.7%), 0.11 m (8.6%), 0.09 m (7.4%), 0.15 m (13.4%), 0.19 m (14.4%), 0.17 m (13.2%), and 0.10 m (8.3%), respectively. The surge at site F was the largest, and at site D was the smallest. The moments of peak wave-induced surge at sites B, C, and H occurred approximately 1 h later than those at other locations. The wave was delayed due to the influence of the geographic location of the YDH.

The largest wave-induced surge occurred at the moment of peak significant wave height (H_s). At this time, wave radiation stress had a greater influence on the water level, and the wave-current interaction was stronger. The peak wave-induced surge occurred later than the peak total surge, but it occurred at almost the same time as the highest water level. The wave-induced surge in the YDH was small. The wave caused an increase of water level at high tide, but a slight decrease of water level at low tide. The wave-induced surge was less significant and occurred later than the wind-induced surge in the YDH.

The peak wave-induced surge in the YDH area occurred at 11 p.m. on July 10 (10 h before landfall). The spatial distributions of the wave-induced surge in the entire model domain and the YDH at this time are shown in Fig. 16. As can be seen from the figure, the impact of the waves on the storm surge was small, particularly in the open sea. A slight surge of around 0.13 m occurred near the Zhejiang coast, while a slight decrease occurred inside Hangzhou Bay. The peak wave-induced surge was about 0.21 m. It occurred on the north shore of the north island chain, due to the shallow water and the bend of the coastline (Fig. 4b). The shelter effect of the islands led to relatively weak waves between the two island chains, which also contributed to the lower surges in the channel, compared with those on the north shore of the north island chain.

Huang et al. (2010) concluded that the wave would result in an additional 0.3–0.5-m increase in water level, compared with that generated only by hurricane. Bertin et al. (2015) pointed out that the wave-induced surge caused by the strong storms Xynthia and Joachim in France’s Biscay Bay exceeded 0.3 m. The results here are very close to their findings.

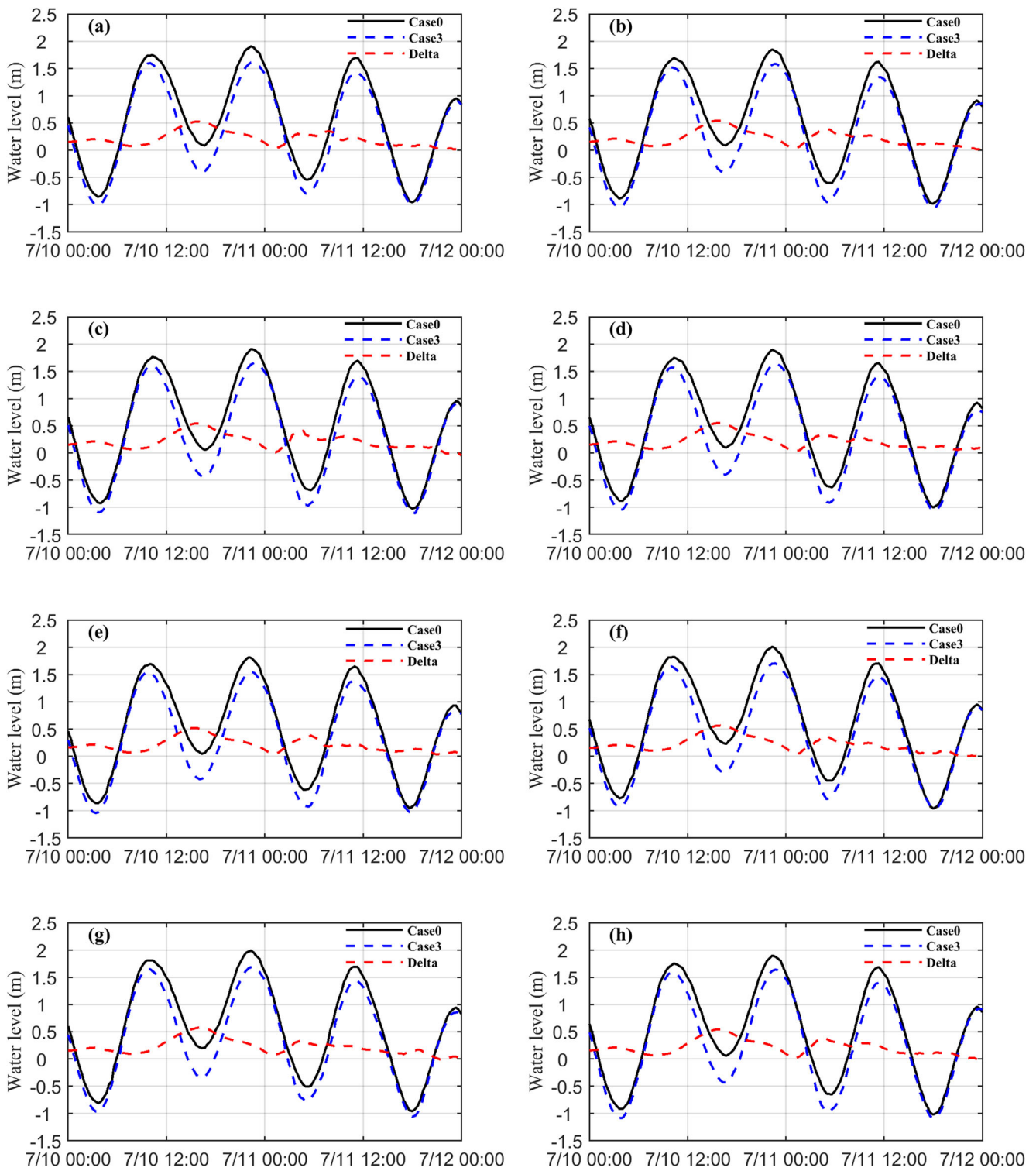


Fig. 17 Water levels of case 1 (black line), case 3 (blue line), and air pressure-induced surge (red line). **a–h** Stations A to H

5.3 Contribution of air pressure to the storm surge in YDH

The air pressure-induced surge was evaluated by comparing the water levels of case 1 and case 3. Figure 17 shows the

water levels in case 1 (black solid line) and case 3 (blue dotted line), and the air pressure-induced surge (red dotted line) at the A to H site (Fig. 4d).

The air pressure-induced surge in the YDH peaked at 5 a.m. on July 11 (4 h before landfall). The air pressure-

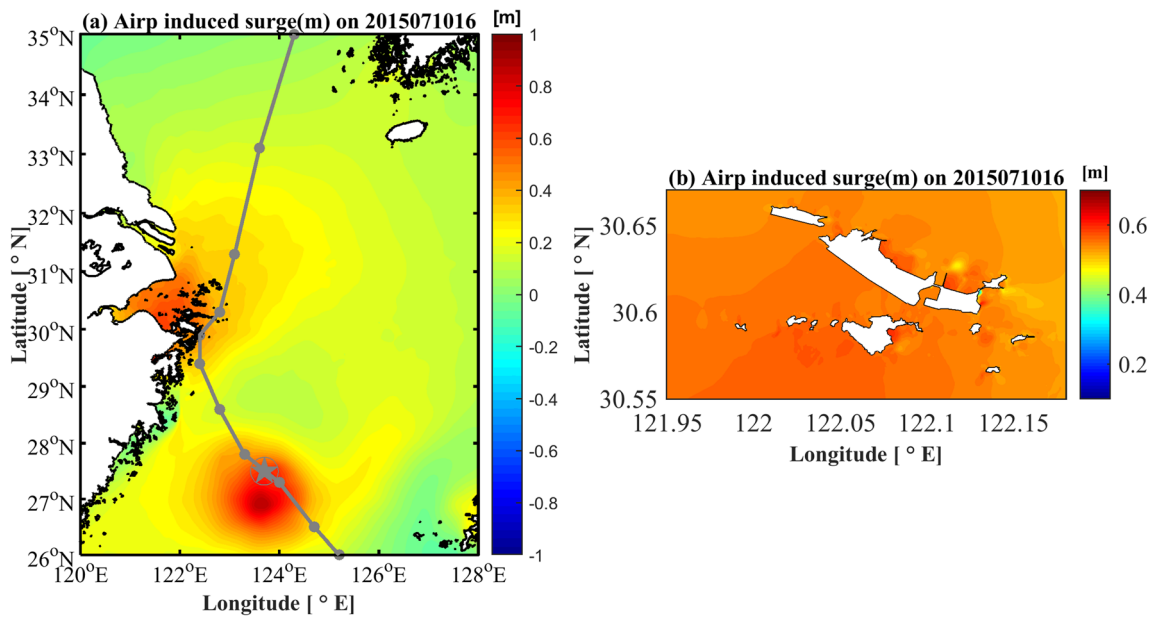


Fig. 18 Spatial distribution of maximum air pressure-induced surge on 5 a.m. July 11: **a** entire model domain and **b** YDH

induced surges at the A to H sites were between 0.27 m and 0.29 m and corresponded to about 22.5%, 22%, 22.1%, 22%, 23.7%, 19.8%, 21.3%, and 23.6% of the total storm surge, respectively. The surge at site H was the largest, and that at site F was the smallest.

The pressure-induced surge had two peaks of almost the same values. The first peak occurred at 4 p.m. on July 10 (17 h before landfall), which was the same moment as the peak of the total surge. The second peak occurred at 5 a.m. on July 11 (4 h before landfall), at the same time as the second peak

Fig. 19 The comparison of the modeled and observed sea surface level. The reconstructed wind data were used in the model (case R1, Table 2)

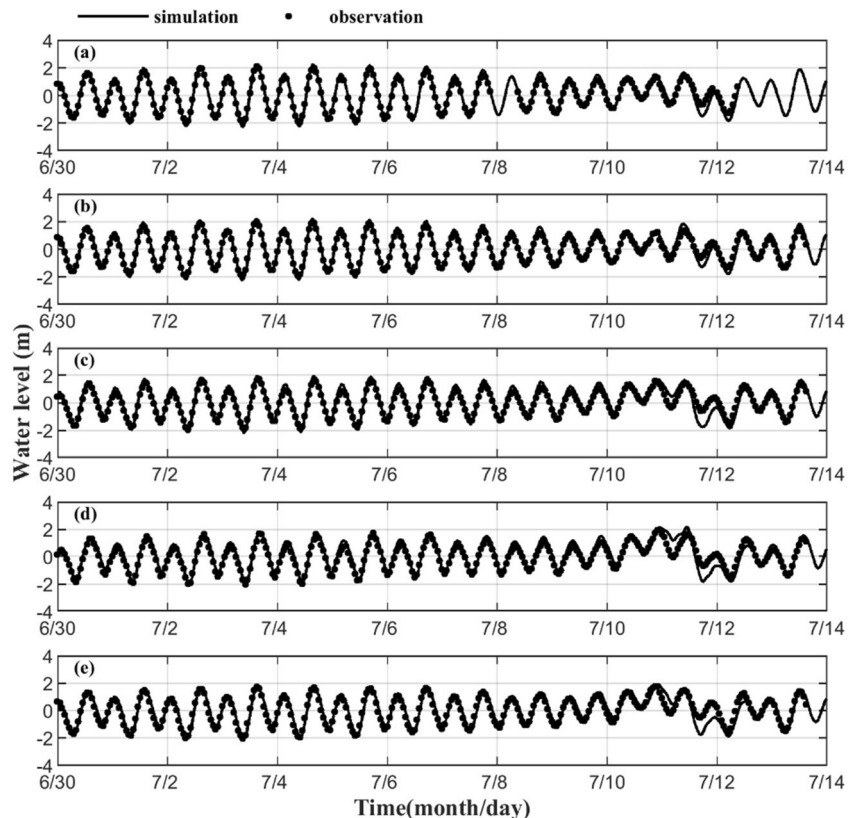
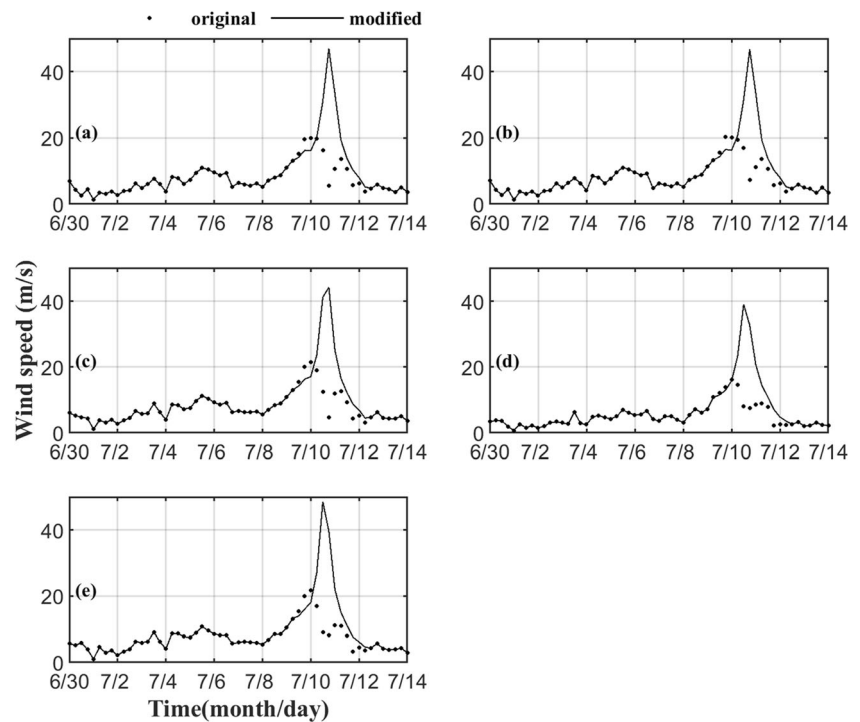


Fig. 20 The comparison of the ECMWF wind data (dotted lines) and the reconstructed wind data (solid lines)



surge. The two pressure-induced surge peaks were both at low tide, and the interval time was exactly one tidal period. These surge peaks were generated by pressure variation and were also impacted by the tide-surge interaction process (Horsburgh and Wilson 2007; Guérin et al. 2018; Zhang et al. 2017).

The peak air pressure-induced surge in the Yangshan sea area appeared at 5 a.m. on July 11 (4 h before landfall). The spatial distributions of the pressure-induced surge in the large sea area and the Yangshan sea area at this time are shown in Fig. 18. As can be seen from the figure, these surges were larger near the Zhejiang coast than in other places (Fig. 18a). The peak pressure-induced surge was about 0.33 m in the YDH (Fig. 18b). The difference of the air pressure-induced surge was very slight in the YDH due to its small area.

5.4 Reconstructed wind data

According to previous studies on storm surges during typhoons (Oey and Chou 2016; Zhang and Oey 2018), the reanalyzed wind data is not appropriate for the simulation of tropical cyclone winds. The data were downloaded, and the wind field was reconstructed according to the method suggested by Oey and Chou (2016) and Zhang and Oey (2018). The wind data were reconstructed using the ECMWF wind data and the Holland algorithm. The reconstructed wind data were used in the model test (case R1, Table 2). However, the calibration of case R1 (Fig. 19) was not as good as the previous results (Fig. 5), particularly during

the storm surges. This is probably because the local bathymetry and local friction were not considered in the Holland algorithm; hence, the peak during the storm surge is larger in the Holland wind data, compared with that in the ECMWF wind data (Fig. 20). The ECMWF wind data were used in this study.

6 Conclusions

The impacts of typhoon Chan-hom on the hydrodynamics in the Yangshan Deep-Water Harbor were studied using a tide-surge-wave coupling numerical model. The model was well calibrated using field data of tidal level, current, and significant wave height. The characteristics of total water level, total storm surge, and current field during typhoon Chan-hom were analyzed. The physical drivers of the storm surge during the typhoon were discussed by numerically investigating the contributions of wind, air pressure, and wave on the storm surge.

Field data showed that Chan-hom landfalls occurred during neap tides. The high water level and the vertical-average currents in the Yangshan area were nearly double those during astronomical tides. The highest water level occurred at the high tide, while the peak surge appeared at low tide. The surge and significant wave height reached 1.3 m and 8 m, respectively, during the typhoon. The maximum vertical averaged current speed was almost 1 m/s. The current directions were almost reversed.

Model results showed total water level to be higher nearer the coast than in the open sea during typhoon Chan-hom. The peak surge occurred at the north coast of the northern island chain due to the backwater by the chain. The flow field in the YDH was slightly southward during typhoon Chan-hom compared with that of an astronomical tide. The flood current in the YDH was weakened. At the ebb tide, the current field was slightly deflected to the south due to the northeast wind.

Several physical processes contribute to the total surge in the YDH. The winds were the most important force (87.1%) behind the peak storm surge, followed by the pressure-induced surge (23.7%). The third force, which contributed about 14.4% to the peak, was the wave-induced surge. The surge in the narrow channel was lower than that in other areas of the YDH. The findings of this study can be applied to similar channel-island systems around the world.

Acknowledgments This study is supported by the National Key Research and Development Program of China (2017YFC0405403), the National Natural Science Foundation of China (11672267, 41606103, 51761135015), and the Zhejiang Provincial Natural Science Foundation of China (LR16E090001).

References

- Bertin X, Li K, Roland A, Bidlot JR (2015) The contribution of short-waves in storm surges: two case studies in the Bay of Biscay. *Cont Shelf Res* 96:1–15
- Brown JM (2010) A case study of combined wave and water levels under storm conditions using WAM and SWAN in a shallow water application. *Ocean Model* 35(3):215–229
- Chen C, Liu H, Beardsley RC (2003) An unstructured, finite-volume, three-dimensional, primitive equation ocean model: application to coastal ocean and estuaries. *J Atmos Ocean Technol* 20(1):159–186
- Chen C, Cowles G, Beardsley RC (2006) An unstructured grid, finite-volume coastal ocean model: FVCOM User Manual SMAST/UMASSD Technical Report-04-0601 (pp. 183).
- Chen C, Beardsley RC, Cowles G, Qi J, Lai ZG, Gao G, Stuebe D (2013) An unstructured grid. FVCOM User Manual, Finite-Volume Community Ocean Model, p 416
- Chen WB, Lin LY, Jang JH, Chang CH (2017) Simulation of typhoon-induced storm tides and wind waves for the north-eastern coast of Taiwan using a tide–surge–wave coupled model. *Water* 9(7):549
- Egbert GD, Erofeeva SY (2002) Efficient inverse modeling of barotropic ocean tides. *Journal of Atmospheric & Oceanic Technology* 19(2): 183–204
- Egbert GD, Bennett AF, Foreman MGG (1994) TOPEX/POSEIDON tides estimated using a global inverse model. *Journal of Geophysical Research Oceans* 99(C12):24821–24852
- Fortunato AB, Freire P, Bertin X, Rodrigues M, Ferreira J, Liberato MLR (2017) A numerical study of the February 15, 1941 storm in the Tagus estuary. *Cont Shelf Res* 144:50–64
- Guérin T, Bertin X, Coulombier T, De Bakker A (2018) Impacts of wave-induced circulation in the surf zone on wave setup. *Ocean Modelling*:S1463500318300246
- Guo W, Wang XH, Ding P, Ge J, Song D (2018) A system shift in tidal choking due to the construction of Yangshan Harbour, Shanghai, China. *Estuar Coast Shelf Sci* 206:49–60
- Horsburgh KJ, Wilson C (2007) Tide-surge interaction and its role in the distribution of surge residuals in the north sea. *J Geophys Res* 112(C8):C08003
- Huang Y, Weisberg RH, Zheng L (2010) Coupling of surge and waves for an Ivan-like hurricane impacting the Tampa Bay, Florida region. *J Geophys Res Oceans* 115(C12)
- Jiang Y, Wu P, Xu J (1999) A study on air pressure action in typhoon surge. *Journal of Oceanography in Taiwan Strait* 4:432–436
- Liu Q, Yu F, Wang P, Dong J (2011) Numerical study on storm surge forecasting considering wave-induced radiation stress. *Acta Oceanol Sin* 33(5):47–53
- Oey L, Chou S (2016) Evidence of rising and poleward shift of storm surge in western North Pacific in recent decades. *J Geophys Res Oceans* 121(7):5181–5192. <https://doi.org/10.1002/2016JC011777>
- Orton P, Georgas N, Blumberg A, Pullen J (2012) Detailed modeling of recent severe storm tides in estuaries of the New York city region. *Journal of Geophysical Research Oceans* 117(C9)
- Pawlowicz R, Beardsley B, Lentz S (2002) Classical tidal harmonic analysis including error estimates in MATLAB using T_TIDE. *Comput Geosci* 28(8):929–937
- Sun Y, Chen C, Beardsley RC, Xu Q, Qi J, Lin H (2013) Impact of current-wave interaction on storm surge simulation: a case study for Hurricane Bob. *Journal of Geophysical Research Oceans* 118(5):2685–2701
- Tolman HL (2010) Effects of numerics on the physics in a third-generation wind-wave model. *J Phys Oceanogr* 22(10):1095–1111
- Warner JC, Geyer WR, Lerczak JA (2005) Numerical modeling of an estuary: a comprehensive skill assessment. *Journal of Geophysical Research Oceans* 110(C5)
- Willmott CJ (1981) On the validation of models. *Physical Geography* 2: 184–194
- Wu, L. Y. (2009). FVCOM-based wave-current-sediment model coupling and its application, PhD thesis, Zhejiang University, China
- Wu, L. Y. (2010). FVCOM-based wave-current-sediment model coupling and its application. Ocean University of China, pp115
- Xie, L., Pietrafesa, L. J., & Wu, K. (1998). A numerical study of wave-current interaction through surface and bottom stresses: coastal ocean response to hurricane Fran of 1996. *Journal of Geophysical Research Oceans*, 108(C2)
- Xie L, Wu K, Pietrafesa L, Zhang C (2001) A numerical study of wave-current interaction through surface and bottom stresses: wind-driven circulation in the South Atlantic bight under uniform winds. *Journal of Geophysical Research Oceans* 106(C8):16841–16855
- Ying M, Zhang W, Yu H, Lu X, Feng J, Fan Y et al (2014) An overview of the China meteorological administration tropical cyclone database. *Journal of Atmospheric & Oceanic Technology* 31(2):287–301
- Zhang MY, Li YS (1996) The synchronous coupling of a third-generation wave model and a two-dimensional storm surge model. *Ocean Eng* 23(6):533–543
- Zhang L, Oey LY (2018) Young ocean waves favor the rapid intensification of tropical cyclones—a global observational analysis. *Mon Weather Rev*. <https://doi.org/10.1175/MWR-D-18-0214.1>
- Zhang H, Cheng W, Qiu X, Feng X, Gong W (2017) Tide-surge interaction along the east coast of the Leizhou peninsula, South China Sea. *Cont Shelf Res* 142:32–49
- Zheng L (2010) Development and application of a numerical model coupling storm surge, tide and wind wave. PhD dissertation, Tsinghua University, Beijing.